JCB Journal of Cell Biology

ARTICLE

Microtubules assemble near most kinetochores during early prometaphase in human cells

Vitali Sikirzhytski[1]*, Fioranna Renda[1]*, Irina Tikhonenko[1], Valentin Magidson[1], Bruce F. McEwen[1], and Alexey Khodjakov[1,2]

For proper segregation during cell division, each chromosome must connect to the poles of the spindle via microtubule bundles termed kinetochore fibers (K-fibers). K-fibers form by two distinct mechanisms: (1) capture of astral microtubules nucleated at the centrosome by the chromosomes' kinetochores or (2) attachment of kinetochores to noncentrosomal microtubules with subsequent transport of the minus ends of these microtubules toward the spindle poles. The relative contributions of these alternative mechanisms to normal spindle assembly remain unknown. In this study, we report that most kinetochores in human cells develop K-fibers via the second mechanism. Correlative light electron microscopy demonstrates that from the onset of spindle assembly, short randomly oriented noncentrosomal microtubules appear in the immediate vicinity of the kinetochores. Initially, these microtubules interact with the kinetochores laterally, but end-on attachments form rapidly in the first 3 min of prometaphase. Conversion from lateral to end-on interactions is impeded upon inhibition of the plus end–directed kinetochore-associated kinesin CenpE.

Introduction

Segregation of chromosomes during cell division requires formation of specialized microtubule bundles termed kinetochore fibers (K-fibers). Mature K-fibers comprise ∼25 microtubules in mammalian cells (McEwen et al., 1997). The dynamic plus ends of these microtubules attach to the kinetochore (Euteneuer and McIntosh, 1981), whereas the minus ends embed into spindle poles or they establish dynamic connections to other microtubule bundles within the spindle (Elting et al., 2014; Sikirzhytski et al., 2014).

Two distinct mechanisms for K-fiber formation have been described (Rieder, 2005; Heald and Khodjakov, 2015). In one mechanism, connection to the pole forms when an astral microtubule produced by a centrosome is captured by a kinetochore. This process has been directly observed in vertebrate cells (Hayden et al., 1990; Merdes and De Mey, 1990; Alexander and Rieder, 1991) and yeast (Tanaka et al., 2005). In the alternative mechanism, K-fibers grow from kinetochores in random directions (Khodjakov et al., 2003; Maiato et al., 2004) until the minus end of a growing fiber is captured and transported poleward along another spindle microtubule by cytoplasmic dynein (Rusan et al., 2002; Maiato et al., 2004; Elting et al., 2014; Sikirzhytski et al., 2014). Kinetochore-driven K-fiber assembly is common in *Drosophila melanogaster* S2 cells (Maiato et al., 2004) and has been occasionally observed in vertebrate cells with prominent centrosomal arrays (Khodjakov et al., 2003). Thus, both mechanisms appear to coexist, but their relative contributions to normal mitosis remain unknown. This lack of information hinders mechanistic understanding and modeling of mitotic spindle assembly. Indeed, kinetochore-driven K-fiber formation is largely ignored in the current computational models of mitosis (Wollman et al., 2005; Paul et al., 2009; Pavin and Tolić-Nørrelykke, 2014; Magidson et al., 2015; Blackwell et al., 2017).

In this study, we demonstrate that at the onset of spindle assembly short noncentrosomal microtubules begin to accumulate near most (>75%) kinetochores in human cells. Initially lateral interactions with these microtubules are rapidly converted into end-on attachments, and the conversion is impeded upon inactivation of the kinetochore-associated kinesin CenpE.

Results

Behavior of Mad2 suggests simultaneous formation of end-on attachments during early prometaphase

The checkpoint protein Mad2 is known to be rapidly removed from the kinetochores when the load-bearing end-on attachments are established (Kuhn and Dumont, 2017). Therefore, the pattern of Mad2 recruitment and release from the kinetochores

[1]Wadsworth Center, New York State Department of Health, Albany, NY; [2]Rensselaer Polytechnic Institute, Troy, NY.

*V. Sikirzhytski and F. Renda contributed equally to this paper; Correspondence to Alexey Khodjakov: alexey.khodjakov@health.ny.gov; V. Magidson's present address is National Cancer Institute, Frederick, MD.

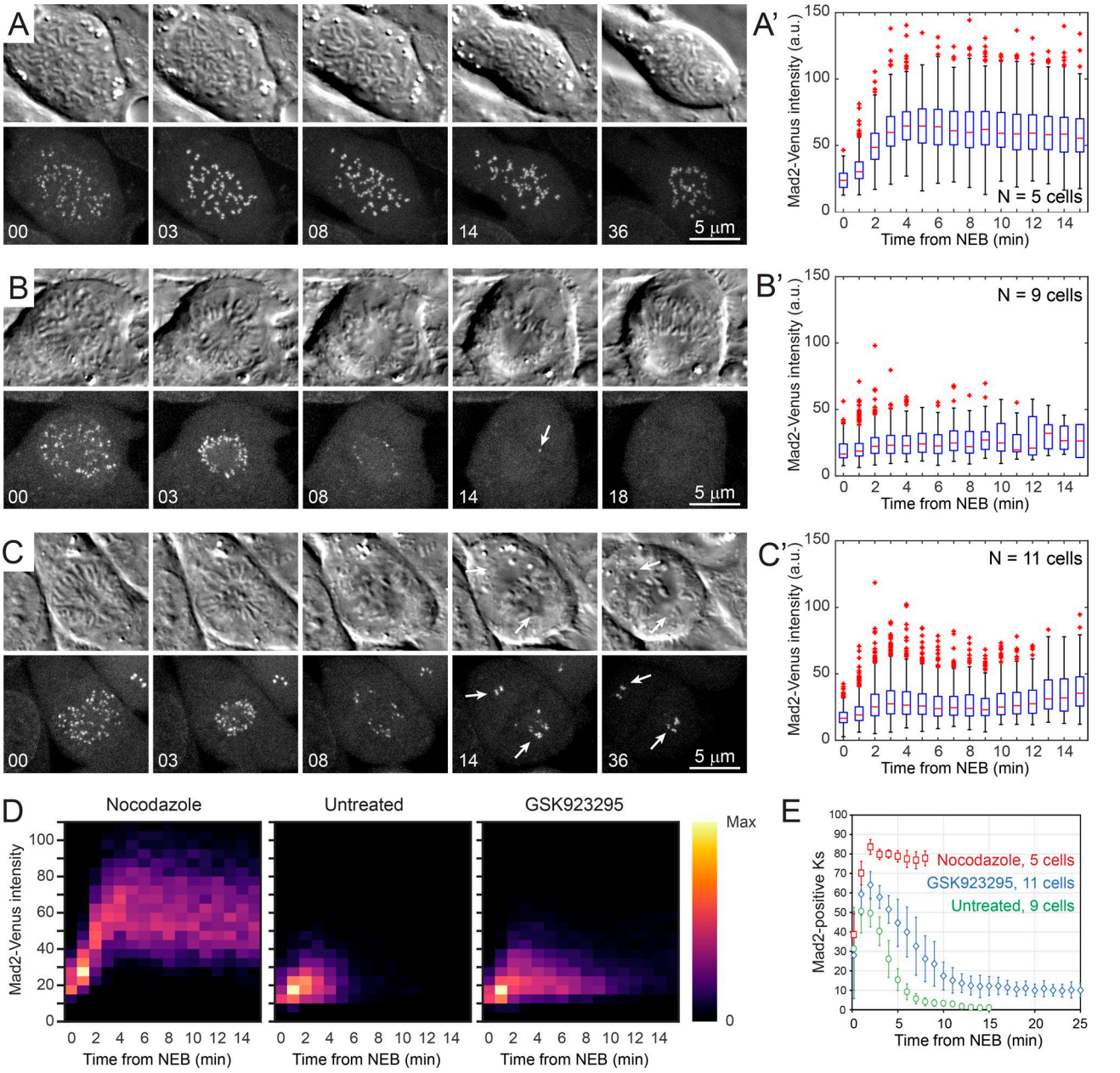

Figure 1. **Behavior of Mad2 during mitosis in RPE1 cells. (A–C)** Selected time points from multimode 3D time-lapse recordings of cells expressing Mad2-Venus. Single focal planes from DIC volumes (top) and maximum-intensity projections of the entire cell (bottom) are shown for each time point (time in minutes from NEB). **(A)** The cell is treated with 3 µM nocodazole to prevent formation of spindle microtubules. **(B)** The cell is under normal culture conditions. Arrow denotes a single Mad2-positive kinetochore that transiently appears ∼4 min before anaphase onset. **(C)** The cell is treated with 20 nM GSK923295 to inhibit CenpE. Arrows point at the perpetually monooriented chromosomes whose kinetochores recruit large amounts of Mad2 at later stages of mitosis. **(A'–C')** Amounts of Mad2 recruited to the kinetochores under the same conditions as in A–C. Each time point is characterized by the median (red marks), range of 25th–75th percentiles (box), full range of the data points (whiskers), and outliers deviating by >2.698 σ from the mean (red crosses). **(D)** Heatmaps presenting distribution of kinetochores with various amounts of Mad2. Lookup tables are normalized to the bins with maximal number of kinetochores in each experimental condition. **(E)** The number of Mad2-positive kinetochores per cell under various conditions. Error bars represent SD.

during spindle assembly is a readout for when most kinetochores become end-on attached.

Time-lapse recordings in RPE1 cells with a single allele of Mad2 replaced with Mad2-Venus (Collin et al., 2013) demonstrate the amount of Mad2 at kinetochores increases for ∼4 min after nuclear envelope breakdown (NEB) and then remains constant in cells entering mitosis without microtubules (3 µM nocodazole; Fig. 1, A and A'; and Video 1).

During normal spindle assembly in untreated cells, microtubules rapidly invade the former nuclear volume while the chromosomes arrange into a ring around the nascent spindle (Fig. 1 B and Video 2; Magidson et al., 2011). The amount of Mad2 recruited to the kinetochores during early prometaphase (1–4 min after NEB) is significantly lower than in nocodazole-treated cells at similar times after NEB (Fig. 1, A' and B'). During late prometaphase-metaphase (>8 min after NEB),

Mad2 may transiently appear at individual kinetochores on fully congressed chromosomes and anaphase is initiated shortly after the last of these "reignited" kinetochores releases Mad2 (Fig. 1 B and Video 2; Saurin et al., 2011; Collin et al., 2013). A large amount of Mad2 is also recruited to the kinetochores of "monooriented" chromosomes that are positioned near the spindle poles. Monoorientation occurs only occasionally (~3% of chromosomes) during normal spindle assembly (Magidson et al., 2011) but becomes frequent upon suppression of the kinetochore-associated kinesin CenpE (kinesin-7). Approximately 10% of chromosomes become perpetually monooriented in cells treated with the CenpE inhibitor GSK923295 (hereafter GSK; Fig. 1 C and Video 3; Gudimchuk et al., 2013; Barisic et al., 2014) or depleted of CenpE via siRNA (Putkey et al., 2002). Suppression of CenpE activity moderately increases the mean value of Mad2 intensity at the kinetochores during early prometaphase (Fig. 1 C′), and this increase of the mean value is primarily caused by a larger number of kinetochores with very high amounts of Mad2 (Fig. 1 C′, red crosses). Mad2 dynamics at the majority of kinetochores are better reflected in heatmaps, where the color of each pixel reflects the number of kinetochores within a certain range of intensities (Fig. 1 D). Heatmaps demonstrate that the amount of Mad2 progressively and synchronously increases at most kinetochores for ~4 min after NEB in nocodazole-treated cells that lack microtubules. When microtubule dynamics are normal, a lower amount of Mad2 is recruited to most kinetochores, and this amount is similar in untreated and GSK-treated cells (Fig. 1 D). In untreated cells, the number of Mad2-positive kinetochores decreases rapidly to <10 kinetochores 6 min after NEB, whereas in GSK-treated cells, the decrease is slower (Fig. 1 E). Numerous kinetochores containing low amount of Mad2 persist during mid-prometaphase (5–8 min after NEB; Fig. 1 D) in cells with inactive CenpE. At later times, Mad2 is present only at the kinetochores of perpetually monooriented chromosomes; however, the amount of Mad2 at these kinetochores is as high as in nocodazole-treated cells (Fig. 1, A and C; 14–36 min).

The observed pattern of Mad2 recruitment and release suggests that during normal spindle assembly, kinetochores begin to interact with microtubules instantly, within the first minute after NEB, and end-on attachments form synchronously on most kinetochores during the early stages of spindle assembly. This behavior is inconsistent with the classic search-and-capture (S&C) mechanism of K-fiber formation based on direct interactions between astral microtubules and unattached kinetochores (Kirschner and Mitchison, 1986; Heald and Khodjakov, 2015). Because of the stochastic nature of S&C, different kinetochores should form end-on attachments at various times. Therefore, the number of Mad2-positive kinetochores is expected to decrease gradually, and many kinetochores should recruit the full amount of Mad2 because of the long time before the initial capture of microtubules. Further, the classic S&C mechanism offers no explanation for the observed changes in the behavior of Mad2 at the kinetochores in GSK-treated cells. Together, these inconsistencies prompted us to structurally characterize microtubule–kinetochore interactions that occur during early prometaphase.

Hotspots of microtubules are adjacent to most kinetochores in early prometaphase

The high density of microtubules within the spindle is a major impediment to visualizing the early stages of K-fiber formation. To overcome this limitation, we used array tomography (AT), an approach where 3D fluorescence volume is reconstructed from independently recorded images of thin serial sections. Elimination of the defocused light normally emitted by the objects in the adjacent focal planes improves the ratio of signal to noise achieved in AT versus conventional light microscopy (LM; Micheva and Smith, 2007; Sikirzhytski et al., 2014).

Reconstructions of early prometaphase cells from 70-nm sections suggest a nonuniform distribution of microtubules within the spindle at the early stages of spindle assembly (Fig. 2 A and Video 4). Microtubules are relatively scarce in the center of the spindle and concentrated in the immediate vicinity of kinetochores (Fig. 2, A and B). To quantitatively assess the density of microtubules in the various parts of the spindle, we used signal averaging. Nine AT volumes were rotated to orient the forming chromosome plates orthogonal to the view axis and translated to superimpose the centers of chromosomal rings (Fig. 3 A). Mean intensity of α-tubulin fluorescence was then characterized within the 210-nm (three voxels)-deep equatorial slice. This analysis demonstrates that microtubule density immediately beneath the chromosome ring is approximately fourfold higher than near the spindle axis (Fig. 3, B and C). This distribution is inconsistent with the idea that the nascent spindle primarily comprises two overlapping astral microtubule arrays generated by the centrosomes and it suggests that additional microtubules form near the centromeres en masse.

Visual evaluation of AT images suggests that small patches of microtubule density exist near the kinetochores. Intensity of α-tubulin fluorescence within 500-nm regions of interest (ROIs), centered on the position of the outer-kinetochore protein CenpF, is greater than the mean intensity of tubulin in the spindle for 77 ± 15% of the kinetochores (749 kinetochores in nine cells). This prompted us to align images of individual kinetochores so that the centers of CenpF are superimposed and the direction toward the center of the spindle is fixed. The intensity of tubulin signal in this averaged dataset is at most ~500 nm from the position of CenpF toward the spindle center (Fig. 3, D and E). This pattern of α-tubulin intensity suggests that either numerous microtubules converge on the kinetochore from multiple directions or that short microtubules accumulate in the immediate vicinity of the kinetochores.

The architecture of the early-prometaphase spindle is not perturbed in GSK-treated cells. Similar to untreated cells, microtubule density is approximately fourfold higher in the area adjacent to the kinetochores than in the center of the spindle (Fig. 3, F and G; 10 averaged AT volumes). However, centromeres in GSK-treated cells are more scattered within a wider ring around the spindle (compare Figs. 3 B with Fig. 3 F). This scattering correlates with a wider peak of α-tubulin density (compare Figs. 3 C with Fig. 3 G), consistent with the notion that microtubules accumulate preferentially near the centromeres. Averaging analysis of kinetochores aligned by the position of CenpF spots suggests that the highest concentration of microtubules exists

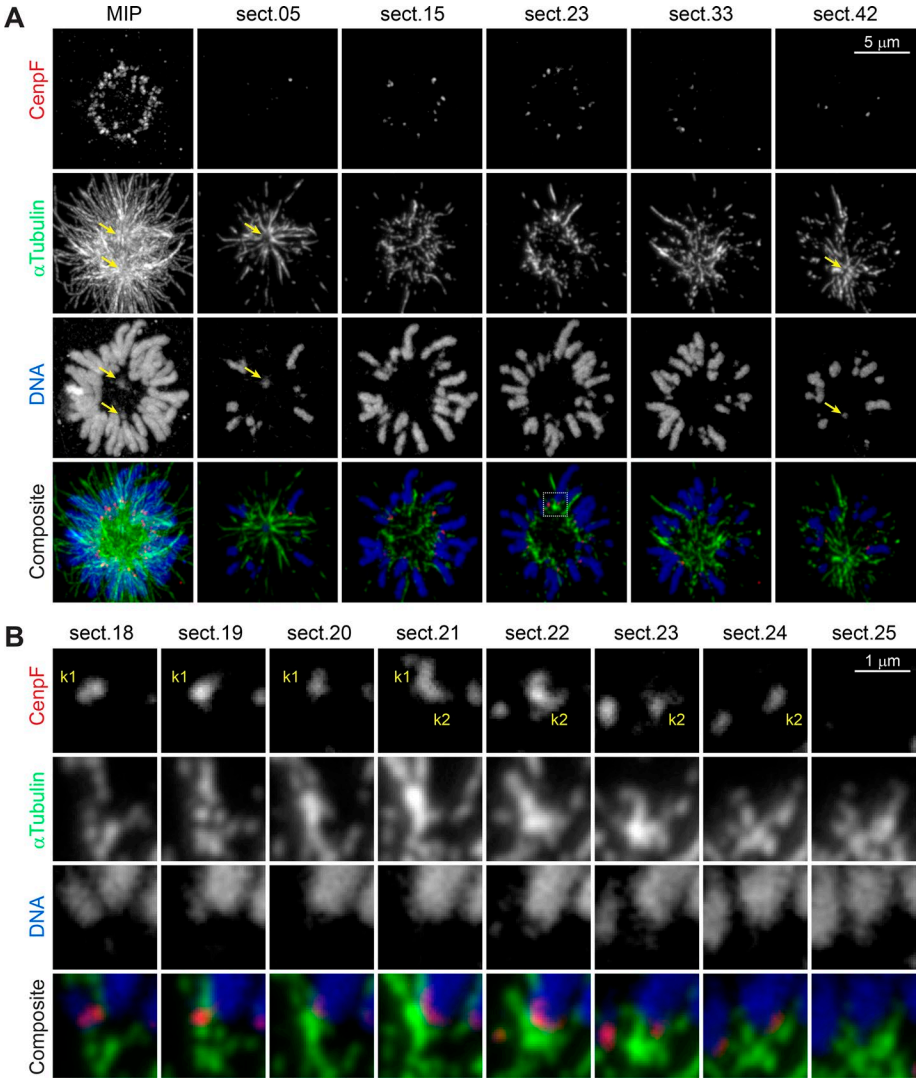

Figure 2. **AT of early-prometaphase RPE1 cell. (A)** Maximum-intensity projection (MIP) of the entire cell volume and selected 70-nm sections depicting kinetochores (CenpF), microtubules (α-tubulin), and DNA (Hoechst 33343). Microtubules radially emanate from the centrosomes (arrows in sect.05, sect.42, and MIP) and extend toward the chromosome ring near the spindle equator (sect.15–sect.33). The density of microtubules is relatively low near the center of the spindle but higher in the area adjacent to the centromeres (sect.23). See Video 1 for full volume of this cell. **(B)** Full series of 70-nm sections through a centromere (box in A, sect.23) at higher magnification. α-Tubulin is highly concentrated near kinetochores. Sister kinetochores (k1 and k2) form a crescent that partially encircles the centromere. Microtubules appear to emanate from the kinetochores but not toward the spindle poles. α-Tubulin concentration is the highest near the kinetochores (sect.21–sect.23).

immediately in front of the kinetochore toward the center of the spindle (Fig. 3, H and I; 853 kinetochores in 10 cells). The peak of α-tubulin intensity is narrower and closer to the position of CenpF in GSK-treated cells than in untreated cells (~200 vs. ~500 nm; Fig. 3, E and I). However, this change may be caused by variability in the scattering of centromeres rather than reflect an actual change in the distance from the kinetochore to the area of highest microtubule concentration.

Accumulation of microtubules near kinetochores begins at NEB, and end-on attachments are present at most kinetochores during early prometaphase

To characterize the distribution of microtubules near kinetochores in greater detail, we capitalized on correlative LM/EM (CLEM). The use of CLEM was necessary because many early-prometaphase kinetochores escape detection in conventional EM as their appearance does not resemble the expected trilaminar plate morphology (unpublished data). To delineate the microtubule-binding domains of all kinetochores, Hec1-tdTomato was ectopically expressed in RPE1 cells with a single allele of the checkpoint gene Mad2 replaced with Mad2-Venus fusion (Fig. 4 A; Collin et al., 2013). This dual-color labeling allowed us to precisely locate individual kinetochores (Video 5) and correlate the character of microtubule–kinetochore interactions with the amount of Mad2 present at a specific kinetochore (Fig. 4, B and C).

Serial-section analysis of 60 kinetochores in two cells reveals that numerous short microtubules reside within 250 nm from the surface of all kinetochores (Fig. 4 D). Indeed, the number of these microtubules (35 ± 13) exceeds the number of microtubules in a mature K-fiber (~25 microtubules; McEwen et al., 1997). Individual microtubules are oriented under a variety of angles to the kinetochore surface (Fig. 4, B and C), but parallel and nearly orthogonal orientations are preferred (Fig. 4 E). The former is expected during lateral interactions between kinetochores and microtubules, whereas the latter is characteristic of end-on attachment. The end-on–attached microtubules emanate from the kinetochore, and some appear to form small bundles that resemble K-fibers. The bundles do not orient toward one of the spindle poles but extend in various directions. The amount of Mad2 at the kinetochore does not correlate with the number of end-on microtubules (Fig. 4 F; Pearson's coefficient $r < 0.1$).

The presence of end-on–attached noncentrosomal microtubules on most kinetochores (56/60) during early prometaphase prompted us to characterize even earlier stages of spindle

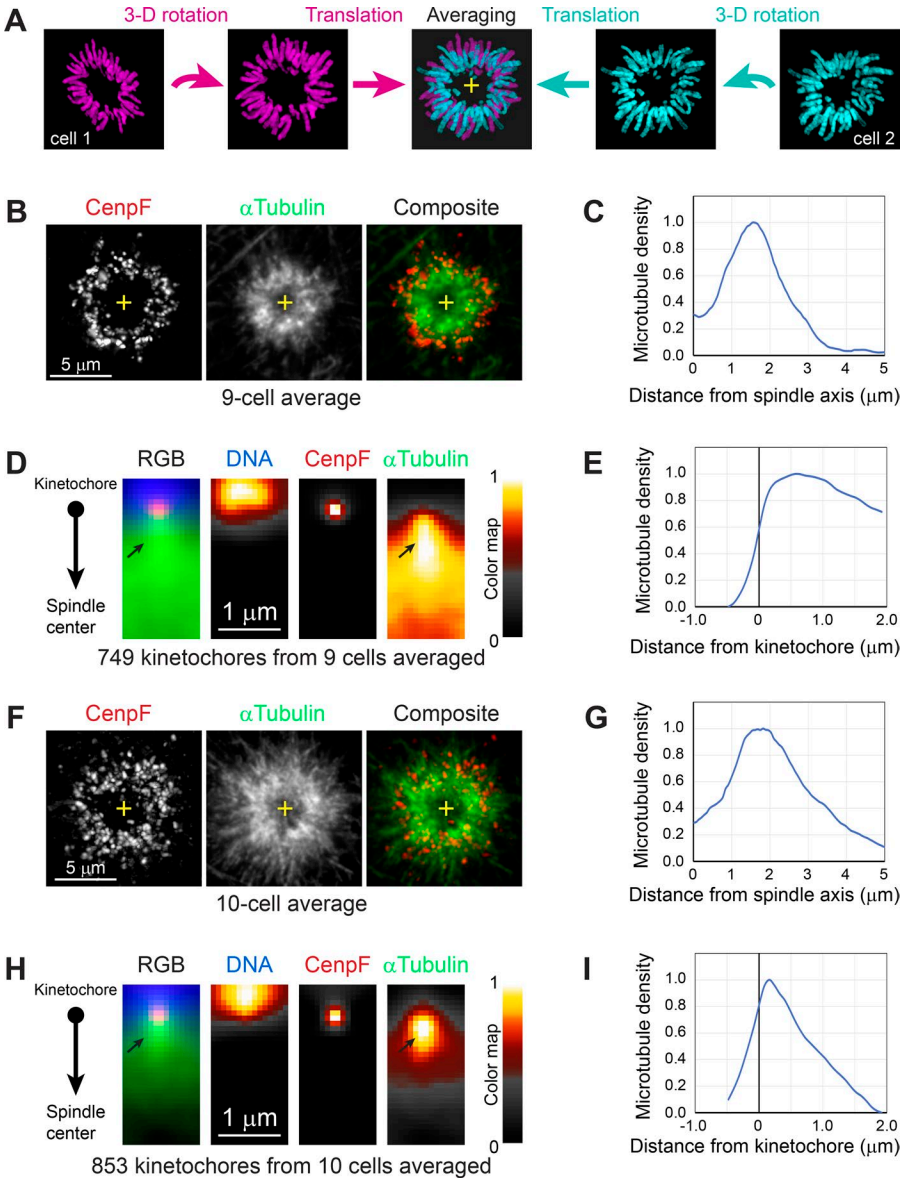

Figure 3. **Mean distributions of kinetochores and microtubules during early prometaphase.** **(A)** Schematics of the alignment approach. Each cell is individually rotated to orient the chromosome ring and translated to fix the position of spindle axis. **(B)** Spatial distribution of kinetochores (CenpF) and microtubules (α-tubulin) within the 210-nm equatorial slice (three 70-nm voxels deep) of the spindle. Images are maximum (CenpF) or mean (α-tubulin) intensity projections of early prometaphase cells rotated to orient the chromosome ring orthogonally to the view axis and translated to superimpose centers of the chromosome rings (crosses). **(C)** Normalized radially averaged α-tubulin intensity distribution profile from the spindle axis (0) toward the cell periphery. The peak is near the ring of centromeres (~1.5 μm from the spindle axis). **(D)** Distribution of α-tubulin intensity near kinetochores. Images are mean intensity projections of kinetochores rotated to fix direction toward the center of the spindle (vertically downward) and translated to superimpose centroids of CenpF (outer kinetochore). Normalized heatmap suggests the highest α-tubulin intensity immediately in front of the kinetochore toward the spindle center (arrows). **(E)** Normalized α-tubulin intensity distribution from the CenpF centroid (0) toward the spindle center. **(F–I)** As in A–D, but the cells were treated with 20 nM GSK923295 to inhibit CenpE.

assembly. AT reconstructions of two cells at the stage when microtubules are beginning to invade the nuclear volume (Figs. 5 A and S1 A) demonstrate that the concentration of α-tubulin is elevated near kinetochores during NEB (Fig. 5 A′). However, the number of kinetochores adjacent to the detectable α-tubulin spots and the intensity of these spots differ significantly between the two analyzed cells as well as within each cell (Fig. 5 B). This variability suggests that accumulation of α-tubulin near kinetochores initiates at a distinct time and proceeds rapidly during the earliest stage of spindle assembly.

EM analysis of two cells with partially disassembled nuclear envelope demonstrates that short microtubules are present near morphologically recognizable kinetochores (Figs. 5 C and S1 B). Most microtubules are short, and their orientation to the kinetochores is highly variable, so that the dense mesh of near-kinetochore microtubule resembles a corona (Fig. 5 C′). Unfortunately, in EM preparations, more than half of kinetochores in RPE1 cells are morphologically indistinct during NEB (Magidson et al., 2015). Therefore, we are unable to quantitatively characterize the distribution of microtubules near kinetochores at the onset of spindle assembly. However, EM strongly suggests that these microtubules are numerous and present at many kinetochores at the earliest stages of spindle assembly.

CenpE promotes formation of end-on attachments during early prometaphase

AT demonstrates that microtubules are abundant near kinetochores when cells enter mitosis with inhibited CenpE (Fig. 3, F and G). However, a slower decay in the amount of Mad2 and the number of Mad2-positive kinetochores in GSK-treated cells (Fig. 1) suggests that inhibition of CenpE impedes transition from the initial lateral interactions to end-on attachments (Shrestha and Draviam, 2013). These observations inspired us to detail the distribution of microtubules near kinetochores during early prometaphase upon chemical inhibition or siRNA depletion of CenpE.

CLEM analysis of five early prometaphase cells with suppressed CenpE activity (three GSK treated and two depleted via

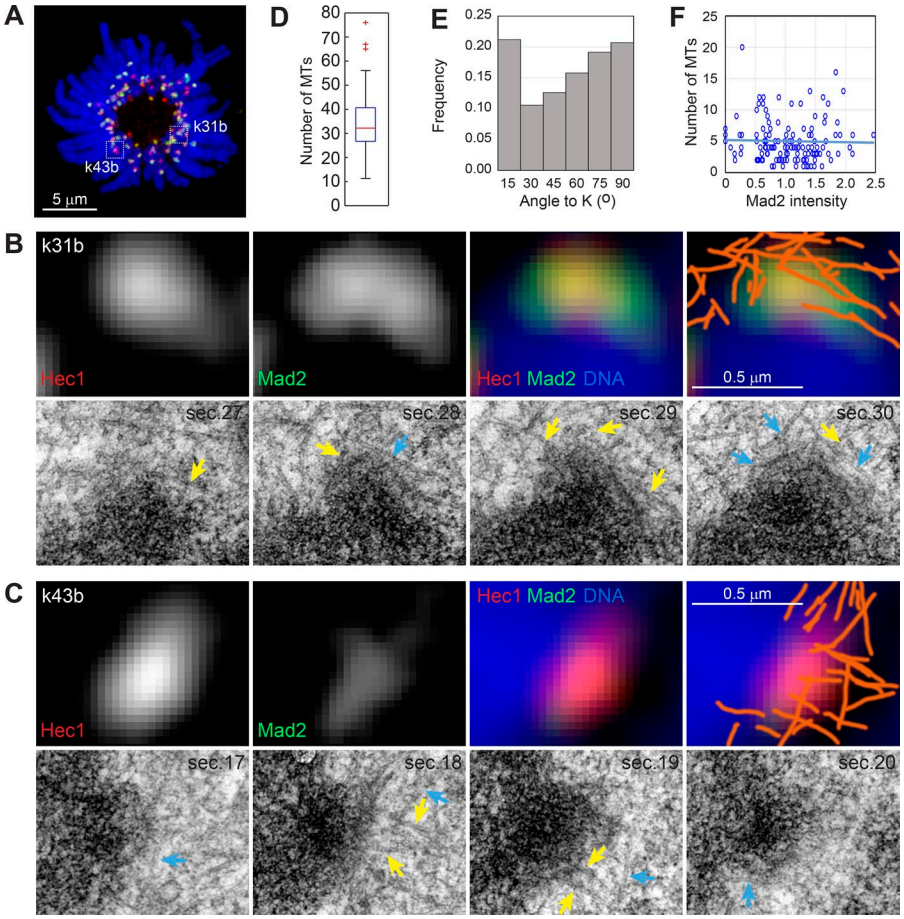

Figure 4. **CLEM characterization of microtubule density near kinetochores during early prometaphase. (A)** Maximum-intensity projection of an early prometaphase cell coexpressing Hec1-tdTomato and Mad2-Venus. Notice highly variable concentration (red vs. yellow) of Mad2 at various kinetochores. See Video 5 for the full volume of this cell with individual kinetochores marked. **(B and C)** LM and correlative EM images of individual kinetochores with intermediate (B) or low (C) amounts of Mad2-Venus. Orange lines demark positions of microtubules traced in EM. Yellow arrows denote end-on–attached microtubules, and blue arrows point at laterally interacting microtubules. **(D)** Tukey box plot presenting the number of microtubules (MTs) within the 250-nm area adjacent to the kinetochore plate (60 kinetochores from two cells; mean = 35). **(E)** Distribution of angles between microtubules and the kinetochore plate. **(F)** Scatterplot presenting the number of end-on–attached microtubules versus the amount of Mad2 at individual kinetochores. Mad2 intensity is normalized so that the background is 0 and the mean value is 1. Regression line slop coefficient = 0.0669 (R^2 = 0.01).

siRNA) proves that CenpE is not required for the accumulation of numerous short microtubules near kinetochores (Fig. 6, A–C; and Fig. S2, A–D). The numbers of microtubules within 250 nm from the kinetochore surface are similar in untreated (35 ± 13) versus CenpE-depleted (34 ± 12) and increased in GSK-treated cells (42 ± 20; P = 0.017 in Student's two-tailed *t* test; Fig. 6 D). This increase may reflect a tighter interaction between kinetochores and microtubule surface because of the rigor binding of the CenpE motor induced by GSK923295 (Wood et al., 2010).

Although end-on attachments are present in the absence of CenpE activity (Figs. 6 C and S2 C), the distribution of angles between microtubules and kinetochores is skewed toward nearly parallel microtubules (Fig. 6 E). Thus, suppression of CenpE activities neither prevents accumulation of short microtubules near kinetochores nor affects lateral interactions. However, end-on attachments to noncentrosomal short microtubules appear to be impeded in the absence of CenpE (compare Figs. 4 E and 6 E).

Like in untreated cells, CLEM analyses reveal no correlation between the number of end-on–attached microtubules and the amount of Mad2-Venus at the kinetochore during early prometaphase (Fig. 6 F; Pearson's coefficient r < 0.1 in both CenpE-inhibited and depleted cells).

Inhibition of CenpE motor activity affects chromosome movements during early prometaphase

Our AT and CLEM analyses demonstrate that from the onset of spindle assembly most kinetochores interact with a dense mesh of short microtubules. Assuming proper polarity, minus ends of end-on–attached microtubules within the mesh would protrude from the kinetochores. Previous work demonstrates that minus ends of short K-fibers protruding from the kinetochores are rapidly connected to the adjacent spindle microtubules by cytoplasmic dynein and this connection supports all types of chromosome movements (Elting et al., 2014; Sikirzhytski et al., 2014). Importantly, kinetochores propelled by dynein-mediated forces at the minus ends of the attached microtubules exhibit characteristic rapid jerks that are not observed in the trajectories of kinetochores directly connected to the spindle poles via continuous K-fibers (Sikirzhytski et al., 2014). Thus, we decided to compare the pattern of kinetochore movements during onset of mitotic spindle assembly in untreated cells versus cells lacking CenpE activity.

3D time lapses recorded at 5-s intervals (Fig. 7 A and Videos 6, 7, and 8) demonstrate that the positions of individual kinetochores in the consecutive frames frequently change by >250-nm (3 pixels) in untreated cells. These momentous jerks occur in various directions, in sharp contrast with the extended linear movements toward the spindle poles (Fig. 7, A and B, arrowheads), and are known to be driven by dynein forces at the kinetochores (Yang et al., 2007). To assess the effect of CenpE inactivation on the frequency of the jerks at the early stages of spindle assembly, we determined the mean position of each kinetochore within rolling 30-s windows (Fig. 7 B) and then calculated the SD for the spread of kinetochore positions in individual frames (Fig. 7 C). This approach is more conservative than direct measurements of

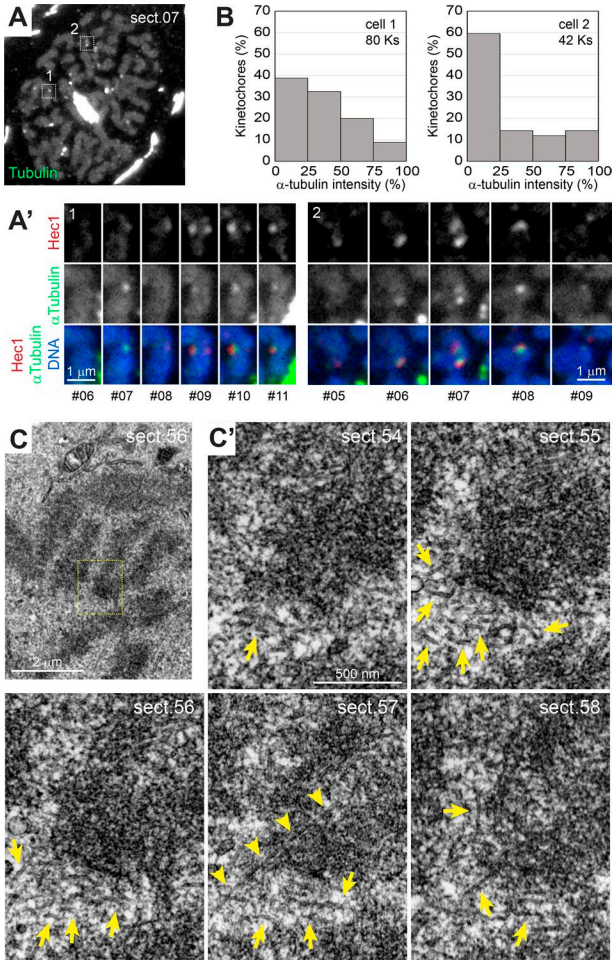

Figure 5. **Accumulation of short microtubules near kinetochores during NEB. (A)** Selected 70-nm section from a full AT series (see Fig. S1 A). Dim spots of α-tubulin are apparent in the immediate proximity of some Hec1 spots if image contrast is increased (linear intensity stretch). **(A')** Full series of sections through centromeres boxed in A. Notice that α-tubulin spots are adjacent to but not precisely colocalized with Hec1 spots. **(B)** Histograms of α-tubulin intensities near kinetochores (Ks) in the two reconstructed cells (cell 1 is the cell shown in A–A'). Intensities are normalized to the brightest spot in each cell. Number of α-tubulin spots detected in each cell is shown. **(C)** 70-nm EM section depicting chromosomes inside a partially perforated nucleus (see Fig. S1 B). **(C')** Full series of EM sections through the centromere boxed in C. Numerous variably oriented microtubules are adjacent to the kinetochores. Most microtubules are short (arrows), but some exceed 1-μm length (arrowheads).

frame-to-frame displacement, which can be affected by inaccurate determination of the kinetochore position in a single frame because of the limited signal-to-noise ratio. Histograms of SD distributions demonstrate that jerky movements are frequent during the initial stages of spindle assembly in untreated cells but are significantly less numerous when CenpE is depleted or chemically inhibited (Fig. 7 C, 0–2 min). Later, the frequency of momentous kinetochore displacements becomes similar in untreated and CenpE-depleted cells; however, these displacements were almost completely suppressed in GSK-treated cells (Fig. 7 C, 2–4 min). The difference in chromosome movements in CenpE-depleted and CenpE-inhibited cells may reflect the rigidity of the microtubule mesh at kinetochores because of the CenpE rigor induced by GSK. Together, these data suggest that interactions between the minus ends of short microtubules protruding from the kinetochores contribute toward chromosome movements and positioning during early prometaphase.

Short microtubules are present near Mad2-positive kinetochores during metaphase

Time-lapse recordings demonstrate that in normal mitoses a low number of kinetochores transiently recruit Mad2 during late prometaphase/metaphase (Fig. 1 B and Video 2). These Mad2-positive kinetochores remain near the spindle equator, which is surprising as chromosomes with a single K-fiber are expected move toward the attached pole at ∼1.5 μm/min (Khodjakov et al., 1997; Sikirzhytski et al., 2014). This prompted us to characterize microtubule interactions of Mad2-positive kinetochores positioned inside fully assembled metaphase plates.

We observe a dense mesh of short microtubules in the immediate proximity of most (7/11) Mad2-positive kinetochores in metaphase RPE1 cells (Fig. 8). These microtubules are variably oriented and they appear to interact with the kinetochore both laterally and end on. Because of the limited sample size and inconspicuous morphology of the outer plate (Fig. 8 C), we are unable to quantitatively characterize the distribution of microtubule angles; however, qualitatively, the mesh of microtubules adjacent to the Mad2-positive kinetochores in metaphase cells resembles that observed during early prometaphase. Importantly, we observe that the microtubule mesh near Mad2-positive kinetochores is also in close proximity to K-fibers connected to kinetochores of other chromosomes (Fig. 8 C).

Discussion

By two methodologically distinct approaches (AT and CLEM), our work demonstrates that from the onset of spindle assembly, most kinetochores in human cells establish contacts with a mesh of short noncentrosomal microtubules accumulating locally near the centromere. The mesh comprises numerous (30–40; Fig. 4) variably oriented and densely packed microtubules (Figs. 4, 5 C, and 6) that interact with the kinetochore laterally as well as end on. The mesh array is likely transient as short randomly oriented microtubules are not observed near kinetochores attached to mature K-fibers (McDonald et al., 1992; McEwen et al., 1997). However, formation of the mesh is not limited to early prometaphase as a similar array of short microtubules appears at the kinetochores that transiently accumulate Mad2 during metaphase (Fig. 8). Rapid formation of the microtubule mesh near unattached kinetochores bears important ramifications for our understanding of the spindle assembly mechanisms.

Nucleation of microtubules near the centromeres has been previously observed in cells recovering from antimicrotubule drugs (Witt et al., 1980; Tulu et al., 2006; Torosantucci et al., 2008; O'Connell et al., 2009). Our analyses of unperturbed human cells alleviate the concern that this phenomenon arose from the artificially high concentration of soluble αβ-tubulin in cells with depolymerized microtubules. Our AT data suggest that microtubules accumulate near most (>75%) kinetochores during early stages of normal spindle assembly, and this number

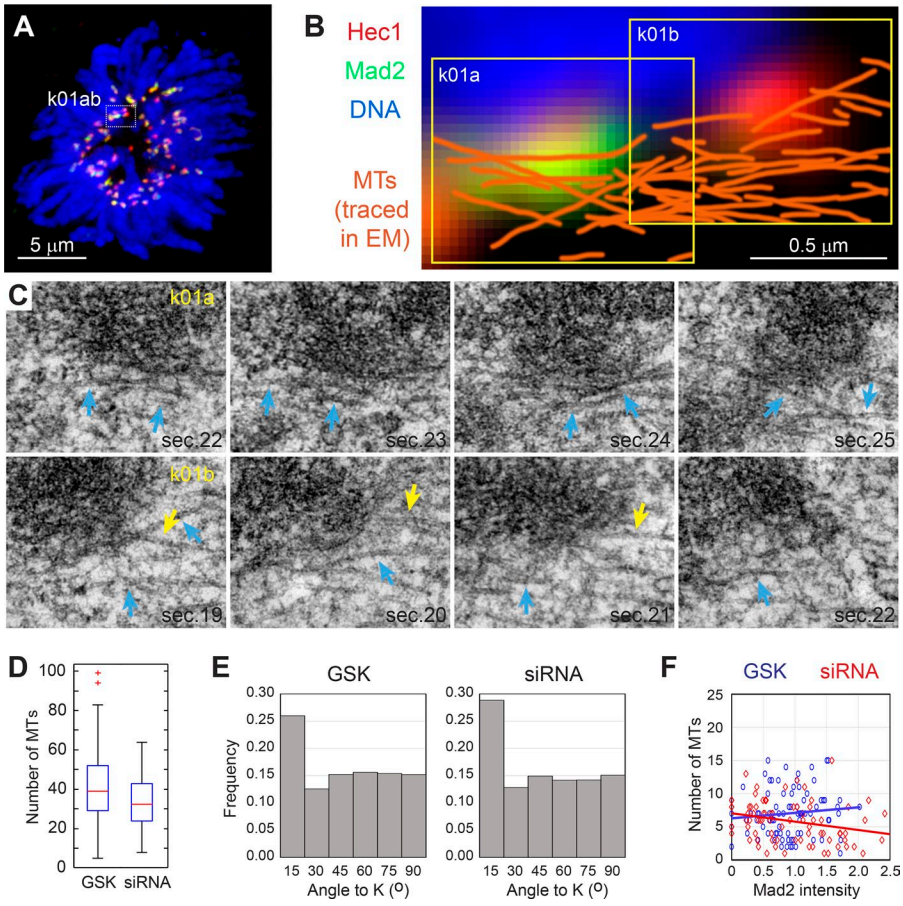

Figure 6. **Effects of CenpE inhibition on interactions of kinetochores with noncentrosomal microtubules during early prometaphase. (A)** Maximum-intensity projection of an early-prometaphase RPE1 cell that entered mitosis in the presence of 20 nM GSK923295. Hec1-tdTomato is shown in red, and Mad2-Venus is shown in green. **(B and C)** Correlative LM (B) and EM (C) images of two sister kinetochores with intermediate (k01a) or low (k01b) amount of Mad2-Venus. Orange lines in B demark positions of microtubules traced in EM. Yellow arrows in C denote end-on–attached microtubules, and blue arrows point at laterally interacting microtubules. **(D)** Tukey box plot presenting the number of microtubules (MTs) within the 250-nm area adjacent to the kinetochore plate in cells with inactive CenpE (GSK; 82 kinetochores from three cells; mean = 42) or depleted of CenpE (siRNA; 83 kinetochores from two cells; mean = 34). **(E)** Distribution of angles between microtubules and the kinetochore plate. The difference between GSK and siRNA distributions is not significant ($P = 0.02$ in two-sample Kolmogorov-Smirnov test); however, both distributions differ from the distribution of angles in untreated cells (Fig. 4 E; $P < 0.001$ in two-sample Kolmogorov-Smirnov test). **(F)** Scatterplot presenting the number of end-on–attached microtubules versus the amount of Mad2 at individual kinetochores. Mad2 intensity is normalized so that the background is 0 and the mean value is 1. The regression line slop coefficient is 0.1863 ($R^2 = 0.05$) for GSK and −1.2453 ($R^2 = 0.09$) for siRNA.

is consistent with observations in cells recovering from spindle poisons (Torosantucci et al., 2008). Thus, kinetochores emerge as major contributors to the initiation of K-fiber formation (Maiato et al., 2004; Kitamura et al., 2010).

Previously, numerous randomly oriented microtubules were observed near kinetochores within seconds after removal of the antitubulin drug colcemid (Witt et al., 1980). At later stages of recovery, these randomly oriented microtubules converted into bundles of end-on–attached microtubules extending from kinetochores in various directions (Witt et al., 1980). Our EM analyses suggest that a similar conversion occurs during normal spindle assembly and that the conversion involves the plus end–directed kinesin CenpE that resides within the outmost peripheral layer of the kinetochore (Wood et al., 1997; McEwen et al., 2001; Kim et al., 2008; Shrestha and Draviam, 2013). Chemical inhibition or siRNA depletion of CenpE suppresses the number of end-on–attached microtubules oriented orthogonally to the kinetochore surface (compare Figs. 4 E and 6 E). In vitro, CenpE has been shown to move processively along a single microtubule and then remain attached to its plus end (Gudimchuk et al., 2013). In the context of microtubule mesh, this activity would transport a short microtubule along the kinetochore surface, delivering its plus end into the kinetochore, where it can become attached with proper polarity (Fig. 9 A). This potential function of CenpE is distinctly different from the role of this motor in driving congression of a few monooriented chromosomes (Kapoor et al., 2006; Kim et al., 2008; Barisic et al., 2015). Indeed, efficient sorting of short microtubules at the kinetochore that results in protrusion of the minus ends outward from the kinetochore would have profound effects on the interactions between the kinetochores and spindle microtubules.

Current models of mitosis primarily focus on the classic description of microtubule capture that involves lateral interactions between an astral microtubule and a “naked” kinetochore (Hayden et al., 1990; Merdes and De Mey, 1990; Rieder and Alexander, 1990). However, in the presence of dense microtubule mesh, astral microtubules approaching a kinetochore may connect either to the kinetochore proper or to the protruding minus ends of mesh microtubules (Fig. 9 B). Two observations reported in this study suggest that the later type of capture occurs frequently. First, we observe the characteristic jerky movements previously attributed to the kinetochores propelled by dynein forces at the minus end of short K-fibers (Sikirzhytski et al., 2014). Second, time-lapse recordings in cells expressing fluorescent Mad2 (Fig. 1) suggest that a temporary loss of K-fiber during metaphase does not result in chromosome monoorientation, which implies that the force that counterbalances the attached sister kinetochore is restored rapidly. Efficient interactions between short K-fibers and spindle microtubules mediated by cytoplasmic dynein have been shown to keep chromosomes near the spindle equator even in the absence of direct connections to the spindle poles (Elting et al., 2014; Sikirzhytski et al., 2014), and our EM analyses demonstrate that short microtubules are consistently present (7 of the 11 analyzed kinetochores) on the Mad2-positive kinetochores that maintain their position within the metaphase plate.

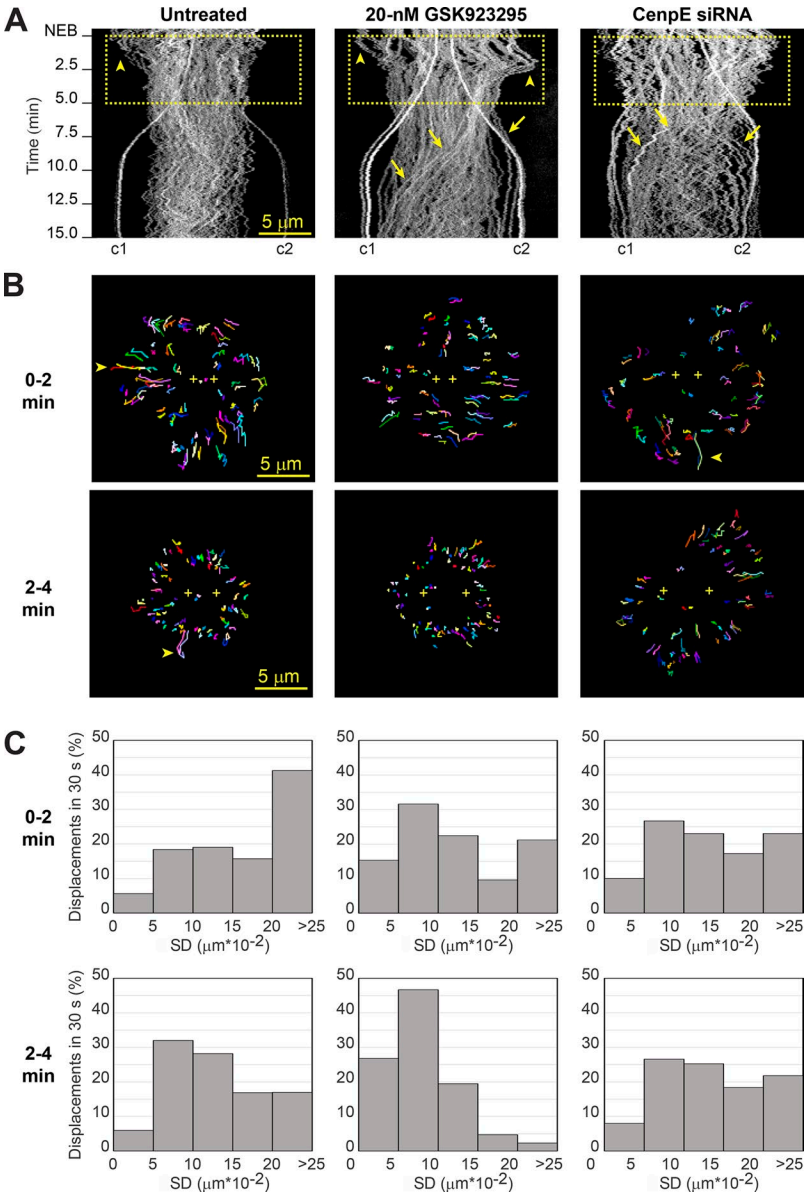

Figure 7. **Effects of CenpE inhibition on kinetochore movements during early prometaphase. (A)** Kymograms generated from aligned 3D volumes of RPE1 cells with GFP-labeled kinetochores (CenpA) and centrioles (Centrin1). In this view, the center of spindle remains stationary and the centrosomes move symmetrically along the horizontal axis so that the pattern of movement with respect to the spindle poles is not obscured by rocking of the spindle within the cell. Arrowheads mark extended rapid movements toward the centrosomes. Arrows point at the extended linear movements that lead to monoorientation of some chromosomes in cells treated with GSK923295 or depleted of CenpE via siRNA (see Videos 6, 7, and 8 for recordings used to generate the kymograms). **(B)** Representative 30 s of kinetochore movements (selected from 0–2 and 2–4 min after NEB). Crosses mark positions of centrosomes. Arrowheads mark rapid movements toward centrosomes sustained for 30 s. **(C)** Histograms of SD values calculated for frame-to-frame (5-s) displacements of individual kinetochores within 30-s rolling windows spanning 0–2 min (top) and 2–4 min (bottom) after NEB. Low SD values (<10 × 10^{-2} µm) correspond with stationary kinetochores, whereas higher SDs (>20 × 10^{-2} µm) indicate jerky movements.

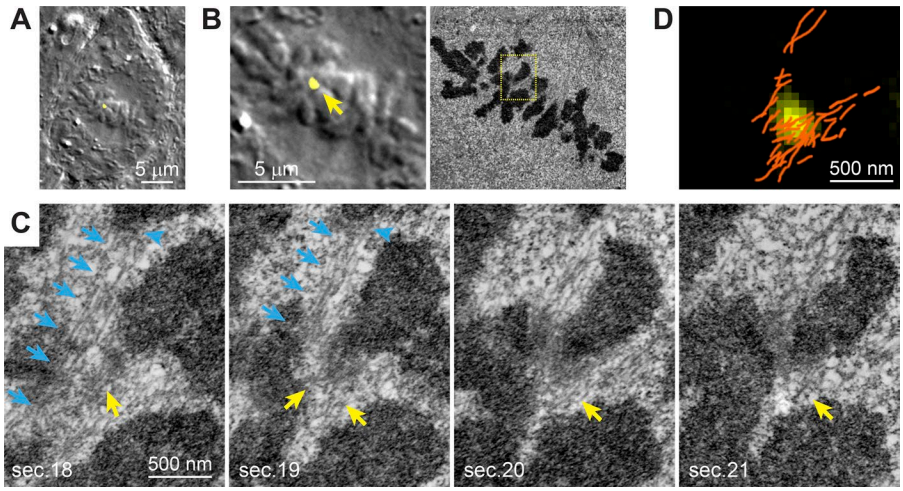

Figure 8. **CLEM characterization of microtubules near Mad2-positive kinetochores during metaphase. (A)** RPE1 cell with fully assembled metaphase plate and a single spot of Mad2-Venus (yellow spot superimposed on gray DIC image). **(B)** Mad2-Venus spot (arrow) corresponds with a single kinetochore. LM (left) and matching EM (right) sections at the same magnification. **(C)** Series of 80-nm sections through the Mad2-positive kinetochore. Yellow arrows point at short microtubules near the kinetochore. Blue arrows denote K-fiber attached to a different kinetochore (arrowheads) and passing near the mesh of short microtubules. **(D)** Superimposition of short microtubules (orange lines; traced in EM) on the LM image of the Mad2-positive kinetochore.

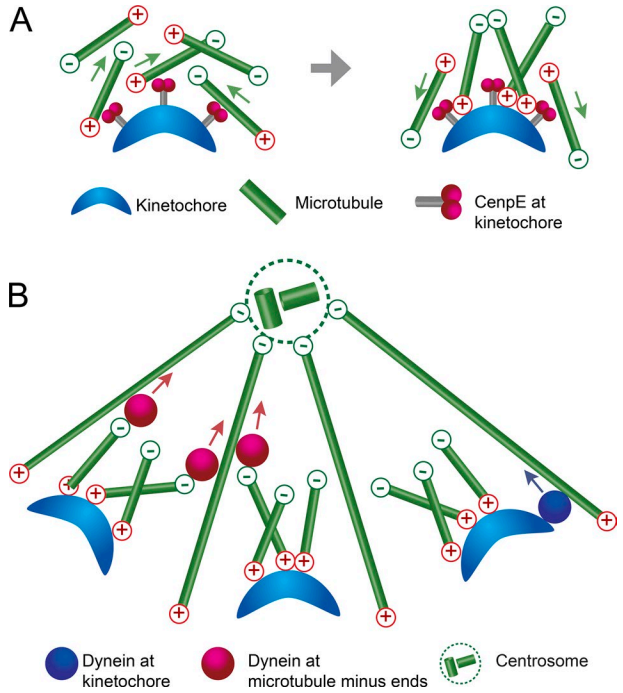

Figure 9. **Ramifications of kinetochore-associated microtubule mesh for the mechanism of spindle assembly. (A)** Plus end–directed motor CenpE facilitates formation of end-on attachments by transporting short microtubules along the kinetochore surface that delivers the plus ends into the kinetochore. As a result of end-on attachments, the minus ends of attached microtubules protrude from the kinetochore. **(B)** Astral microtubules approaching kinetochores may connect directly to the kinetochore surface or the minus ends of protruding short microtubules. Although either connection leads to a poleward force because of dynein activity, the force is generated at distinctly different locales: kinetochore proper versus distal ends of attached microtubules. A dense mesh of microtubules forming at early stages of spindle assembly increases the probability of the latter type of interaction.

Together, our data support the notion that K-fiber formation is initiated by the CenpE-mediated conversion of lateral contacts with noncentrosomal microtubules nucleated near kinetochores and that subsequent attachment to the spindle poles is driven by the dynein-mediated forces acting at the minus ends of these nascent K-fibers.

Materials and methods

Cell culture and fluorescent protein expression

Immortalized hTERT-RPE1 cells were purchased from Takara Bio Inc. at passage 118.5, and then frozen stocks were prepared at passages 120–123 and kept in liquid nitrogen. Passages 130–140 were used in all experiments. The cells remain chromosomally stable at these passages as evident from the presence of 46–47 kinetochore pairs in every cell reconstructed by AT or CLEM. Stable expression of CenpA-GFP and centrin1-GFP in hTERT-RPE1 (Takara Bio Inc.) cells was achieved by transfection with lentivirus as described previously (Magidson et al., 2011). The same clones were used for tracking chromosome movement in this work and previous publications (Magidson et al., 2011; Sikirzhytski et al., 2014).

Immortalized hTERT-RPE1 cells with a single allele of Mad2 replaced with Mad2-Venus (Collin et al., 2013) were a gift from J. Pines (Institute for Cancer Research, London, England, UK). Plasmid DNA encoding full-length Hec1 (Guimaraes et al., 2008), a gift from J. DeLuca (Colorado State University, Fort Collins, CO) tagged with tdTomato (a gift from M. Davidson, Florida State University, Tallahassee, FL; plasmid 54653; Addgene) was transiently transfected into these cells (10 µg DNA per ∼300,000 cells) by electroporation with Nucleofector kit V (Lonza VCA-1003 X-001 program; Amaxa Biosystems) 48 h before fixation. All cell cultures were grown in antibiotic-free DMEM supplemented with 10% FCS (Thermo Fisher Scientific) at 37°C and 5% CO_2. Routine in-house test results for mycoplasma were negative.

Drug treatments and siRNA depletion

Microtubule depolymerization was induced by 3 µM nocodazole (Sigma-Aldrich). Motor activity of CenpE was inhibited by GSK-923295 (Haoyuan Chemexpress) at 20 nM final concentration. Drugs were added to the growth medium as 1,000× stock solutions in DMSO. Live imaging or fixation was performed after 2.5 h of exposure to the drug.

CENP-E siRNA duplex (5′-AAGGCUACAAUGGUACUAUAU-3′; Kapoor et al., 2006) was purchased from GE Healthcare. The oligonucleotide and Hec1-tdTomato plasmid were cotransfected into RPE1 cells by electroporation with a Nucleofector (X-005 program; Amaxa Biosystems). Depletion efficiency was assessed by Western blot in whole-cell lysates collected 48 h after cotransfection.

Western blot membranes were cut into upper and lower-molecular-weight parts and probed with mouse monoclonal anti–CENP-E (1H12; ab5093; Abcam) and anti–α tubulin (DM1A; T9026; Sigma-Aldrich) antibodies, respectively. Primary antibodies were followed by HRP-conjugated anti–mouse IgGs (ab97023; Abcam), and staining was detected using an ECL detection kit (REF 34577 SuperSignal; Thermo Fisher Scientific). Depletion efficiency was calculated by normalizing raw intensity of CenpE staining with the intensities of α-tubulin bands in the same lane.

Time-lapse recordings

Cells expressing GFP- or Venus-tagged proteins were grown on #1.5 glass coverslips for 24–48 h and subsequently mounted in Rose chambers containing CO_2-independent medium (Thermo Fisher Scientific) supplemented with 10% FCS. The chambers were maintained at 37°C on the microscope stage. Cells were imaged on a Nikon TE-2000E2 Perfect Focus System microscope equipped with a 100× Plan Apochromat 1.4 NA oil-immersion objective lens (Nikon) in spinning-disk confocal mode (CSU-22; Yokogawa Electric Corporation). Images were captured on a back-illuminated charge-coupled device (CCD) camera (iXon-897 electron-multiplying CCD; Andor Technology) at 107-nm X-Y pixel size. Multimode (fluorescence and differential interference contrast [DIC]) recordings were done at 30–60 s intervals at 500-nm z steps for fluorescence and 1,000-nm z steps for DIC. Higher–temporal resolution fluorescence recordings were obtained at 5-s intervals at 500-nm z steps (15 planes). The system was controlled by IQ software (Andor Technology).

Analysis of Mad2 dynamics in time-lapse recordings

Coordinates of Mad2-positive kinetochores were determined in Imaris (9.1.2; Bitplane) using the Spots tool. These coordinates

were then transferred into ImageJ (National Institutes of Health), and mean pixel intensities were calculated for 7 × 7–pixel ROIs centered on each kinetochore. The raw intensity was corrected by background subtraction and photobleaching compensation. Bleaching curves were calculated individually for each recording by measuring mean fluorescence intensity within nuclei of interphase cells adjacent to the mitotic cell of interest. Statistical analyses and construction of heatmaps were done in MAT LAB (MathWorks).

Analysis of kinetochore movement

To analyze chromosome movements, we first tracked 3D positions of mother centrioles and then rotated the 3D volume at each time point to fix the position of their center and the orientation of the spindle. The rotation was done in FIJI (ImageJ) through two sequential steps, rotation in x–y plane (around the z axis) followed by rotation around the x axis. This processing allowed us to observe chromosome movement in the precisely transverse and axial views of the spindle. Original 3D volumes were scaled to obtain isotropic voxels. Mother centrioles were then tracked using MTrackJ plugin (FIJI). Oriented isotropic 3D volumes were then imported into Imaris for detection and tracking of the kinetochores. We find that prealignment of the spindles to achieve a stable viewpoint of 3D volume facilitates tracking because the trajectories are not affected the constant rocking of the spindle. Fully automatic tracking in Imaris proved to be impractical because of frequent errors in connecting tracks of neighboring kinetochores.

3D coordinates of centrosomes and kinetochore pairs were subsequently transferred into MATLAB for further analysis. Because most kinetochores are not directly connected to a spindle pole during early prometaphase, kinetochore–pole distances were determined to the centriole that was the closer to the kinetochore in the last frame of the recording. SD of distances between kinetochores and centrosomes were calculated independently for each track using a 30-s moving window. Distributions of SD values for control and GSK-treated cells were compared using a two-sample Kolmogorov–Smirnov test with the null hypothesis that the correspondent datasets are from the same continuous distribution.

AT and analysis of tubulin distribution

RPE1 cells in a confluent monolayer were lysed in warm PEM buffer (100 mM Pipes, pH 6.9, 2.5 mM EGTA, and 5 mM $MgCl_2$, pH 6.9) supplemented with 1% Triton-X100 for 1 min before fixation with 1% glutaraldehyde (G5882; Sigma-Aldrich) for 10 min in PEM. Microtubules were visualized with DM1α monoclonal anti–α-tubulin antibody at 1:100 (T9026; Sigma-Aldrich) followed by a secondary antibody conjugated with Alexa Fluor 488 (A-11029; Thermo Fisher Scientific). Outer kinetochores were stained with a rabbit polyclonal antibody against a C-terminal peptide of CenpF (NB500-101; Novus Biological) at 1:50 followed by a secondary antibody conjugated with Alexa Fluor 594 (A-11037; Thermo Fisher Scientific). After immunostaining, cells were postfixed with 2% paraformaldehyde (EM grade; Electron Microscopy Sciences) for 5 min, rinsed with PBS, and kept overnight at 4°C in PBS with 1 µg/ml Hoechst 33343 to stain DNA (chromosomes). Cells were then embedded in LR white resin following conventional protocols. The resin was polymerized at 58°C for 20 h. A full series of 70-nm sections was obtained for early prometaphase cells selected after embedding under a phase contrast microscope (Optiphot; 20× and 60× optics equipped with QuadFluor fluorescence attachment; Nikon). The sections were adhered to #1.5 coverslips, dried, and mounted in glycerol.

Multimode images (phase contrast and three-color fluorescence) were collected on a Nikon TE2000E2 microscope equipped with Plan Apochromat 100× 1.45 NA objective lens and 1.4 NA trans-illumination condenser. The latter was necessary to collect inherently coregistered high-resolution phase contrast and fluorescent images for each section. Images were recorded on a Zyla 4.2 PLUS sCMOS camera (Andor Technology) at 43-nm pixel size.

Cell volumes were reconstructed by roughly aligning sequential sections in Photoshop (CS4; Adobe) using morphological features such as the contour of the cell and positions of organelles prominent in phase-contrast images. This initial alignment was subsequently refined in ImageJ using the MultiStackReg plugin. For subsequent analysis, rotational and translational alignment of different cells was done using the approach described in the Analysis of kinetochore movement section.

For the analysis of α-tubulin intensity distribution within the spindle, 3D volumes of each cell were rotated so that the ring formed by the centromeres rested in the horizontal plane. Radial distributions of microtubules were calculated using the 3D radial distribution tool of ImageJ Suite applied to the 210-nm-deep subvolume that included the central part of the centromere ring.

To characterize α-tubulin distribution near kinetochores, individual kinetochores were rotated in 3D to fix the orientation of the vector from this kinetochore to the center of the spindle. Kinetochore positions were defined by the centroids of CenpF spots, and the position of spindle center was determined as the center of the line connecting the poles. Mean intensity of α-tubulin was measured within a 1 × 1–µm ROI centered on the kinetochore. Mean intensity of α-tubulin within the spindle was calculated by for the volume encircled by the chromosomes.

Quantification of α-tubulin intensity near kinetochores during NEB was limited to the kinetochores residing away from astral microtubules. Mean pixel intensity was calculated within 7 × 7–pixel ROI centered on the α-tubulin spots adjacent to Hec1 spots. Background intensity values were obtained by averaging the mean intensity within three 7 × 7–pixel ROIs in the vicinity of the α-tubulin spot.

CLEM

Cells were fixed in 2.5% glutaraldehyde (Sigma-Aldrich) in 0.1 M cacodylate buffer, pH 7.4 (Electron Microscopy Sciences), and mounted in Rose chambers with imaging media composed of 0.1 M cacodylate buffer, pH 7.4, EC-Oxyrase (diluted 1:100; Sigma-Aldrich), 15 mM lactic acid (Sigma-Aldrich), and 0.1 µg/ml Hoechst 33343. This imaging media was necessary to obtain sufficient signals for both GFP (green) and Venus (yellow) fluorescence. Multimode (DIC and three-color fluorescence) datasets were obtained on a Nikon TE2000 microscope equipped with a Plan Apochromat 100× 1.45 NA objective lens. Images were recorded on an iXon-885 electron-multiplying CCD camera

(Andor Technology) at 53-nm x–y pixel size and 200-nm z steps. All images were deconvolved in SoftWoRx 5.0 software (Applied Precision Ltd.) with lens-specific point spread functions.

Postfixation, embedding, and sectioning were done as previously described (Rieder and Cassels, 1999). Thin sections (70–80 nm) were imaged on JEOL 1400 microscope operated at 80 kV using side-mounted 4.0-megapixel XR401 sCMOS camera (Advanced Microscopy Techniques) controlled by AMT Capture Engine ver.7.0. Full series of images recorded at 10,000× magnification were used to reconstruct the volume of the cell and match orientation and superimpose this volume on the corresponding LM dataset. Serial EM images were then collected for individual kinetochores that yielded unobstructed view in both LM and EM datasets. These high-magnification images were subsequently used to trace microtubules and analyze their distribution.

Contours of kinetochores and microtubules were traced in five adjacent sections within 1 × 1 µm ROIs centered on the geometrical centers of the outlined kinetochores. The contours were delineated using the segmented line tool (spline fit mode) in ImageJ. Minimal distances between kinetochore and microtubule ROIs and angles between microtubules and the kinetochore surface were calculated in ImageJ (using a custom ImageJ Macro script). Results were transferred into MATLAB and Excel (Microsoft) for statistical analyses.

Statistical analyses

All box plots (Fig. 1, A′–C′; Fig. 4 D; and Fig. 6 D) show the median (mark), 25th–75th percentiles (box), full range of the data points (whiskers), and outliers deviating by >2.698 σ from the mean (crosses). The significance of differences in the number of microtubules (Figs. 4 D and 5 D) was assessed using homoscedastic two-tailed Student t tests. Distributions of microtubule angles (Figs. 4 E and 6 E) were compared using two-sample Kolmogorov–Smirnov tests. The correlation between the number of end-on–attached microtubules and the amount of Mad2 (Figs. 4 and 5) was assessed using Pearson's coefficient (Pearson product-moment correlation coefficient).

Preparation of illustrations

LM images were scaled without interpolation in ImageJ to match the final magnification of EM images. Contrast and brightness of the final images were linearly adjusted in Photoshop (CS6) and the figures assembled in Illustrator (CS6; Adobe). Graphs were prepared in MATLAB or Excel and imported into Illustrator as PDFs.

Online supplemental material

Fig. S1 presents proof that kinetochores shown in Fig. 5 are from cells fixed at the onset of spindle assembly. Fig. S2 presents CLEM images that support numeric data shown in Fig. 6. Videos 1, 2, and 3 present recordings used to generate data presented Fig. 1. Videos 4 and 5 present full 3D volumes of cells shown in Figs. 2 and 4. Videos 6, 7, and 8 present recordings used to generate data shown in Fig. 7.

Acknowledgments

EM was enabled by the use of the Wadsworth Center's Electron Microscopy Core Facility.

This work was supported by National Institutes of Health grant GM059363 (to A. Khodjakov).

The authors declare no competing financial interests.

Author contributions: V. Sikirzhytski and A. Khodjakov designed the experiments and analysis techniques. V. Sikirzhytski, F. Renda, and V. Magidson conducted experiments and collected and analyzed the data. I. Tikhonenko prepared EM and AT samples. B.F. McEwen conducted independent verification of EM data. A. Khodjakov wrote the manuscript with significant input from all authors.

Submitted: 16 October 2017
Revised: 15 April 2018
Accepted: 21 May 2018

References

Alexander, S.P., and C.L. Rieder. 1991. Chromosome motion during attachment to the vertebrate spindle: initial saltatory-like behavior of chromosomes and quantitative analysis of force production by nascent kinetochore fibers. *J. Cell Biol.* 113:805–815. https://doi.org/10.1083/jcb.113.4.805

Barisic, M., P. Aguiar, S. Geley, and H. Maiato. 2014. Kinetochore motors drive congression of peripheral polar chromosomes by overcoming random arm-ejection forces. *Nat. Cell Biol.* 16:1249–1256. https://doi.org/10.1038/ncb3060

Barisic, M., R. Silva e Sousa, S.K. Tripathy, M.M. Magiera, A.V. Zaytsev, A.L. Pereira, C. Janke, E.L. Grishchuk, and H. Maiato. 2015. Mitosis. Microtubule detyrosination guides chromosomes during mitosis. *Science.* 348:799–803. https://doi.org/10.1126/science.aaa5175

Blackwell, R., O. Sweezy-Schindler, C. Edelmaier, Z.R. Gergely, P.J. Flynn, S. Montes, A. Crapo, A. Doostan, J.R. McIntosh, M.A. Glaser, and M.D. Betterton. 2017. Contributions of Microtubule Dynamic Instability and Rotational Diffusion to Kinetochore Capture. *Biophys. J.* 112:552–563. https://doi.org/10.1016/j.bpj.2016.09.006

Collin, P., O. Nashchekina, R. Walker, and J. Pines. 2013. The spindle assembly checkpoint works like a rheostat rather than a toggle switch. *Nat. Cell Biol.* 15:1378–1385. https://doi.org/10.1038/ncb2855

Elting, M.W., C.L. Hueschen, D.B. Udy, and S. Dumont. 2014. Force on spindle microtubule minus ends moves chromosomes. *J. Cell Biol.* 206:245–256. https://doi.org/10.1083/jcb.201401091

Euteneuer, U., and J.R. McIntosh. 1981. Structural polarity of kinetochore microtubules in PtK1 cells. *J. Cell Biol.* 89:338–345. https://doi.org/10.1083/jcb.89.2.338

Gudimchuk, N., B. Vitre, Y. Kim, A. Kiyatkin, D.W. Cleveland, F.I. Ataullakhanov, and E.L. Grishchuk. 2013. Kinetochore kinesin CENP-E is a processive bi-directional tracker of dynamic microtubule tips. *Nat. Cell Biol.* 15:1079–1088. https://doi.org/10.1038/ncb2831

Guimaraes, G.J., Y. Dong, B.F. McEwen, and J.G. Deluca. 2008. Kinetochore-microtubule attachment relies on the disordered N-terminal tail domain of Hec1. *Curr. Biol.* 18:1778–1784. https://doi.org/10.1016/j.cub.2008.08.012

Hayden, J.H., S.S. Bowser, and C.L. Rieder. 1990. Kinetochores capture astral microtubules during chromosome attachment to the mitotic spindle: direct visualization in live newt lung cells. *J. Cell Biol.* 111:1039–1045. https://doi.org/10.1083/jcb.111.3.1039

Heald, R., and A. Khodjakov. 2015. Thirty years of search and capture: The complex simplicity of mitotic spindle assembly. *J. Cell Biol.* 211:1103–1111. https://doi.org/10.1083/jcb.201510015

Kapoor, T.M., M.A. Lampson, P. Hergert, L. Cameron, D. Cimini, E.D. Salmon, B.F. McEwen, and A. Khodjakov. 2006. Chromosomes can congress to the metaphase plate before biorientation. *Science.* 311:388–391. https://doi.org/10.1126/science.1122142

Khodjakov, A., R.W. Cole, B.F. McEwen, K.F. Buttle, and C.L. Rieder. 1997. Chromosome fragments possessing only one kinetochore can congress to the spindle equator. *J. Cell Biol.* 136:229–240. https://doi.org/10.1083/jcb.136.2.229

Khodjakov, A., L. Copenagle, M.B. Gordon, D.A. Compton, and T.M. Kapoor. 2003. Minus-end capture of preformed kinetochore fibers contributes to spindle morphogenesis. *J. Cell Biol.* 160:671–683. https://doi.org/10.1083/jcb.200208143

Kim, Y., J.E. Heuser, C.M. Waterman, and D.W. Cleveland. 2008. CENP-E combines a slow, processive motor and a flexible coiled coil to produce an essential motile kinetochore tether. *J. Cell Biol.* 181:411–419. https://doi.org/10.1083/jcb.200802189

Kirschner, M., and T. Mitchison. 1986. Beyond self-assembly: from microtubules to morphogenesis. *Cell.* 45:329–342. https://doi.org/10.1016/0092-8674(86)90318-1

Kitamura, E., K. Tanaka, S. Komoto, Y. Kitamura, C. Antony, and T.U. Tanaka. 2010. Kinetochores generate microtubules with distal plus ends: their roles and limited lifetime in mitosis. *Dev. Cell.* 18:248–259. https://doi.org/10.1016/j.devcel.2009.12.018

Kuhn, J., and S. Dumont. 2017. Spindle assembly checkpoint satisfaction occurs via end-on but not lateral attachments under tension. *J. Cell Biol.* 216:1533–1542. https://doi.org/10.1083/jcb.201611104

Magidson, V., C.B. O'Connell, J. Lončarek, R. Paul, A. Mogilner, and A. Khodjakov. 2011. The spatial arrangement of chromosomes during prometaphase facilitates spindle assembly. *Cell.* 146:555–567. https://doi.org/10.1016/j.cell.2011.07.012

Magidson, V., R. Paul, N. Yang, J.G. Ault, C.B. O'Connell, I. Tikhonenko, B.F. McEwen, A. Mogilner, and A. Khodjakov. 2015. Adaptive changes in the kinetochore architecture facilitate proper spindle assembly. *Nat. Cell Biol.* 17:1134–1144. https://doi.org/10.1038/ncb3223

Maiato, H., C.L. Rieder, and A. Khodjakov. 2004. Kinetochore-driven formation of kinetochore fibers contributes to spindle assembly during animal mitosis. *J. Cell Biol.* 167:831–840. https://doi.org/10.1083/jcb.200407090

McDonald, K.L., E.T. O'Toole, D.N. Mastronarde, and J.R. McIntosh. 1992. Kinetochore microtubules in PTK cells. *J. Cell Biol.* 118:369–383. https://doi.org/10.1083/jcb.118.2.369

McEwen, B.F., A.B. Heagle, G.O. Cassels, K.F. Buttle, and C.L. Rieder. 1997. Kinetochore fiber maturation in PtK1 cells and its implications for the mechanisms of chromosome congression and anaphase onset. *J. Cell Biol.* 137:1567–1580. https://doi.org/10.1083/jcb.137.7.1567

McEwen, B.F., G.K. Chan, B. Zubrowski, M.S. Savoian, M.T. Sauer, and T.J. Yen. 2001. CENP-E is essential for reliable bioriented spindle attachment, but chromosome alignment can be achieved via redundant mechanisms in mammalian cells. *Mol. Biol. Cell.* 12:2776–2789. https://doi.org/10.1091/mbc.12.9.2776

Merdes, A., and J. De Mey. 1990. The mechanism of kinetochore-spindle attachment and polewards movement analyzed in PtK2 cells at the prophase-prometaphase transition. *Eur. J. Cell Biol.* 53:313–325.

Micheva, K.D., and S.J. Smith. 2007. Array tomography: a new tool for imaging the molecular architecture and ultrastructure of neural circuits. *Neuron.* 55:25–36. https://doi.org/10.1016/j.neuron.2007.06.014

O'Connell, C.B., J. Loncarek, P. Kaláb, and A. Khodjakov. 2009. Relative contributions of chromatin and kinetochores to mitotic spindle assembly. *J. Cell Biol.* 187:43–51. https://doi.org/10.1083/jcb.200903076

Paul, R., R. Wollman, W.T. Silkworth, I.K. Nardi, D. Cimini, and A. Mogilner. 2009. Computer simulations predict that chromosome movements and rotations accelerate mitotic spindle assembly without compromising accuracy. *Proc. Natl. Acad. Sci. USA.* 106:15708–15713. https://doi.org/10.1073/pnas.0908261106

Pavin, N., and I.M. Tolić-Nørrelykke. 2014. Swinging a sword: how microtubules search for their targets. *Syst. Synth. Biol.* 8:179–186. https://doi.org/10.1007/s11693-014-9134-x

Putkey, F.R., T. Cramer, M.K. Morphew, A.D. Silk, R.S. Johnson, J.R. McIntosh, and D.W. Cleveland. 2002. Unstable kinetochore-microtubule capture and chromosomal instability following deletion of CENP-E. *Dev. Cell.* 3:351–365. https://doi.org/10.1016/S1534-5807(02)00255-1

Rieder, C.L. 2005. Kinetochore fiber formation in animal somatic cells: dueling mechanisms come to a draw. *Chromosoma.* 114:310–318. https://doi.org/10.1007/s00412-005-0028-2

Rieder, C.L., and S.P. Alexander. 1990. Kinetochores are transported poleward along a single astral microtubule during chromosome attachment to the spindle in newt lung cells. *J. Cell Biol.* 110:81–95. https://doi.org/10.1083/jcb.110.1.81

Rieder, C.L., and G. Cassels. 1999. Correlative light and electron microscopy of mitotic cells in monolayer cultures. *Methods Cell Biol.* 61:297–315. https://doi.org/10.1016/S0091-679X(08)61987-1

Rusan, N.M., U.S. Tulu, C. Fagerstrom, and P. Wadsworth. 2002. Reorganization of the microtubule array in prophase/prometaphase requires cytoplasmic dynein-dependent microtubule transport. *J. Cell Biol.* 158:997–1003. https://doi.org/10.1083/jcb.200204109

Saurin, A.T., M.S. van der Waal, R.H. Medema, S.M. Lens, and G.J. Kops. 2011. Aurora B potentiates Mps1 activation to ensure rapid checkpoint establishment at the onset of mitosis. *Nat. Commun.* 2:316. https://doi.org/10.1038/ncomms1319

Shrestha, R.L., and V.M. Draviam. 2013. Lateral to end-on conversion of chromosome-microtubule attachment requires kinesins CENP-E and MCAK. *Curr. Biol.* 23:1514–1526. https://doi.org/10.1016/j.cub.2013.06.040

Sikirzhytski, V., V. Magidson, J.B. Steinman, J. He, M. Le Berre, I. Tikhonenko, J.G. Ault, B.F. McEwen, J.K. Chen, H. Sui, et al. 2014. Direct kinetochore-spindle pole connections are not required for chromosome segregation. *J. Cell Biol.* 206:231–243. https://doi.org/10.1083/jcb.201401090

Tanaka, K., N. Mukae, H. Dewar, M. van Breugel, E.K. James, A.R. Prescott, C. Antony, and T.U. Tanaka. 2005. Molecular mechanisms of kinetochore capture by spindle microtubules. *Nature.* 434:987–994. https://doi.org/10.1038/nature03483

Torosantucci, L., M. De Luca, G. Guarguaglini, P. Lavia, and F. Degrassi. 2008. Localized RanGTP accumulation promotes microtubule nucleation at kinetochores in somatic mammalian cells. *Mol. Biol. Cell.* 19:1873–1882. https://doi.org/10.1091/mbc.e07-10-1050

Tulu, U.S., C. Fagerstrom, N.P. Ferenz, and P. Wadsworth. 2006. Molecular requirements for kinetochore-associated microtubule formation in mammalian cells. *Curr. Biol.* 16:536–541. https://doi.org/10.1016/j.cub.2006.01.060

Witt, P.L., H. Ris, and G.G. Borisy. 1980. Origin of kinetochore microtubules in Chinese hamster ovary cells. *Chromosoma.* 81:483–505. https://doi.org/10.1007/BF00368158

Wollman, R., E.N. Cytrynbaum, J.T. Jones, T. Meyer, J.M. Scholey, and A. Mogilner. 2005. Efficient chromosome capture requires a bias in the 'search-and-capture' process during mitotic-spindle assembly. *Curr. Biol.* 15:828–832. https://doi.org/10.1016/j.cub.2005.03.019

Wood, K.W., R. Sakowicz, L.S.B. Goldstein, and D.W. Cleveland. 1997. CENP-E is a plus end-directed kinetochore motor required for metaphase chromosome alignment. *Cell.* 91:357–366. https://doi.org/10.1016/S0092-8674(00)80419-5

Wood, K.W., L. Lad, L. Luo, X. Qian, S.D. Knight, N. Nevins, K. Brejc, D. Sutton, A.G. Gilmartin, P.R. Chua, et al. 2010. Antitumor activity of an allosteric inhibitor of centromere-associated protein-E. *Proc. Natl. Acad. Sci. USA.* 107:5839–5844. https://doi.org/10.1073/pnas.0915068107

Yang, Z., U.S. Tulu, P. Wadsworth, and C.L. Rieder. 2007. Kinetochore dynein is required for chromosome motion and congression independent of the spindle checkpoint. *Curr. Biol.* 17:973–980. https://doi.org/10.1016/j.cub.2007.04.056